



Article

Attraction in Action: Reduction of Water to Dihydrogen Using Surface-Functionalized TiO₂ Nanoparticles

Sven A. Freimann, Catherine E. Housecroft and Edwin C. Constable *

Department of Chemistry, University of Basel, Mattenstrasse 24a, BPR 1096, 4058 Basel, Switzerland; s.freimann@unibas.ch (S.A.F.); catherine.housecroft@unibas.ch (C.E.H.)

* Correspondence: edwin.constable@unibas.ch

Abstract: The reactivity of a heterogeneous rhodium(III) and ruthenium(II) complex-functionalized TiO₂ nanoparticle (NP) system is reported. The ruthenium and rhodium metal complexes work in tandem on the TiO₂ NPs surface to generate H₂ through water reduction under simulated and normal sunlight irradiation. The functionalized TiO₂ NPs outperformed previously reported homogeneous systems in turnover number (TON) and frequency (TOF). The influence of individual components within the system, such as pH, additive, and catalyst, were tested. The NP material was characterized using TGA-MS, ¹H NMR spectroscopy, FTIR spectroscopy, solid absorption spectroscopy, and ICP-MS. Gas chromatography was used to determine the reaction kinetics and recyclability of the NP-supported photocatalyst.

Keywords: nanoparticles; anchored-catalyst; heterogeneous catalysis; water reduction

Citation: Freimann, S.A.; Housecroft, C.E.; Constable, E.C. Attraction in Action: Reduction of Water to Dihydrogen Using Surface-Functionalized TiO₂ Nanoparticles. *Nanomaterials* **2022**, *12*, 789. <https://doi.org/10.3390/nano12050789>

Academic Editor: Chung-Li Dong

Received: 20 January 2022

Accepted: 24 February 2022

Published: 25 February 2022

Publisher's Note: MDPI stays neutral with regard to jurisdictional claims in published maps and institutional affiliations.



Copyright: © 2022 by the authors. Licensee MDPI, Basel, Switzerland. This article is an open access article distributed under the terms and conditions of the Creative Commons Attribution (CC BY) license (<https://creativecommons.org/licenses/by/4.0/>).

1. Introduction

The increasing energy demand of the world population has led to the unsustainable consumption of fossil fuels and emission of greenhouse gases [1–3]. Within the next century, fossil fuels will be substantially depleted if consumption rates or energy sources do not change [4]. The development of cleaner, renewable, available, and less-expensive energy solutions has become a central societal and research imperative [5].

Dihydrogen is an outstanding candidate as fuel, possessing key advantages, including long term storage and carbon-free combustion. Liquid or high-pressure gaseous dihydrogen has high gravimetric energy density while lacking volumetric energy density compared to liquid fossil fuels [6]. Hydrogen is the most abundant element in the universe and the tenth most abundant element in the earth's crust by weight percentage. Terrestrially, only small amounts of elemental H₂ occur, with most hydrogen found within molecules, most commonly water [7]. This means dihydrogen for use as fuel must be generated through chemical transformations.

The most common processes for large-scale dihydrogen preparation are water electrolysis and steam methane reforming [8]. Both technologies require high amounts of energy and work best with non-sustainable metal catalysts [8–10]. An imperative is improving energy efficiency and using sustainable, recyclable, or easily recoverable catalysts [11]. One option is to combine energy harvesting and dihydrogen evolution using photocatalysts that work under sunlight irradiation [12].

Homogeneous photocatalytic systems can be very efficient, although catalyst recovery can be extremely challenging and cost or energy-intensive [13,14]. In particular, multicomponent systems are problematic. Heterogeneous catalysts are often easier to recover but have the disadvantage of inactive interior volumes with only surface sites being catalytically active [13–15]. An alternative is to surface-functionalize nanoparticle (NP) scaffolds composed of cheap and abundant elements with photocatalysts. Such immobilized photocatalysts offer greater catalyst-to-volume ratios than bulk heterogeneous catalysts,

which translates to enhanced catalytic activity and turnover. An additional benefit of NPs is the ability to disperse them in liquid phases [16–19]. A number of heterogeneous NP photocatalytic systems, including CdS NPs [20], Cu-doped TiO₂ NPs [21] or ZnO NPs [22], Pt-doped TiO₂ NPs [23] or ZnO NPs [24], Ti³⁺ doped TiO₂ NPs [25], and TiO₂ mediated ligand-capped RuO₂ NPs [26], have been reported as efficient systems for dihydrogen generation. Results of comparable systems are summarized in Table 1.

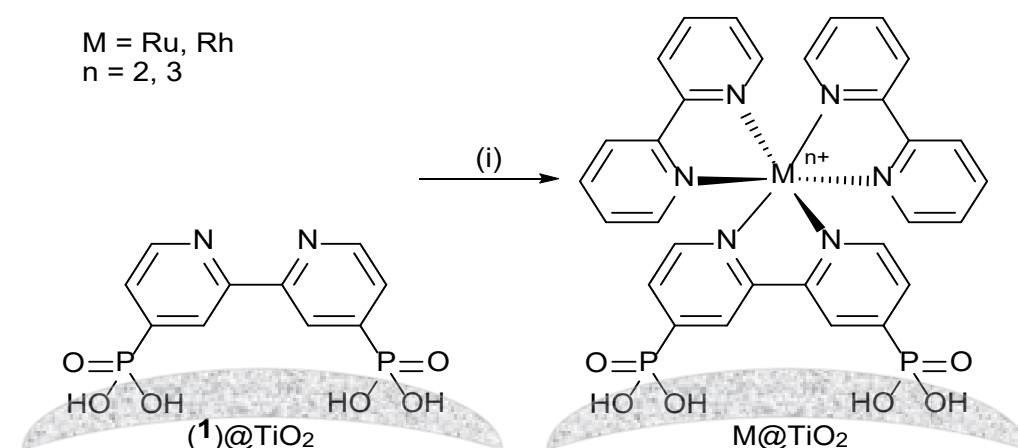
We now describe the immobilization of components from a previously reported aqueous photochemical system for water reduction under simulated sunlight irradiation [27]. The system utilizes TiO₂ NPs supporting ruthenium(II) and rhodium(III) 2,2'-bipyridine (bpy) complexes as photosensitizer and relay species, respectively Scheme 1) [27]. The complexes at the desired surface ratio are assembled on [2,2'-bipyridine]-4,4'-diylbis(phosphonic acid) (**1**) functionalized NPs (**1**@TiO₂). Comparative studies with ZrO₂ NPs are also reported. ZrO₂ is an insulator and the NPs are commercially available. The change from TiO₂ (band gap = 3.2 eV) [28] to ZrO₂ (band gap = 5.1 eV) [29] was expected to yield insights into metal complex to NP surface bonding and electronic interactions.

Table 1. Comparative H₂ evolution materials in the literature.

System	Cat _A / μmol	Cat _B / μmol	Irr./ h	Yield H ₂ / μmol	TON _A	TOF _A / h ⁻¹	TON _B	TOF _B / h ⁻¹
CdS ^a [20]	1730	-	6	283	0.2	0.0	-	-
TiO ₂ p25 ^a [20]	3130	-	6	62	0.0	0.0	-	-
0.25%Pt@TiO ₂ ^b [23]	1.3	-	3	432	337	112.4	-	-
0.75%Pt@ZnO ^c [24]	3.8	-	3	745	194	64.6	-	-
Ru@RuO ₂ PPTiO ₂ -RuP ^d [26]	0.6	-	10	111	176	17.6	-	-
Ru(bpy) ₃ ²⁺ , Rh(bpy) ₃ ³⁺ ^e [27]	1.8	11.7	32	1359	748	23.4	116	3.6

^a Using TEOA (0.67 M) as electron donor, ^b using TEOA (0.25 M) as electron donor and Eosin Y as dye at 1:83 to photocatalyst, ^c using TEOA (0.76 M) as electron donor and Eosin Y as dye at 1:2 to photocatalyst, ^d using TEOA (0.2 M) as electron donor, ^e using TEOA (0.42 M) as electron donor and K₂[PtCl₄] (0.28 mM) as catalyst.

The NPs were characterized using Fourier-transform infrared (FTIR) and solid-state absorption spectroscopies, thermogravimetric analysis mass spectrometry (TGA-MS), triple quadrupole inductively coupled plasma mass spectrometry (ICP-QQQ-MS), and matrix-assisted laser desorption/ionization (MALDI) mass spectrometry while dihydrogen generation was analysed using gas chromatography (GC, see ESI† for details).



Scheme 1. Assembly of metal complexes on TiO₂ NPs starting from NPs functionalized with **1**. Conditions: (i) MCl₃·3H₂O (M = Ru or Rh), bpy, EtOH: H₂O, 160 °C, autoclave, 1 h.

2. Materials and Methods

2.1. General

$\text{RuCl}_3 \cdot 3\text{H}_2\text{O}$ was purchased from Oxkem Ltd., Reading, UK. $\text{RhCl}_3 \cdot 3\text{H}_2\text{O}$ was purchased from Johnson Matthey, Materials Technology UK. 2,2'-Bipyridine and triethanolamine (TEOA) were purchased from Apollo Scientific Ltd., Stockport, UK and Sigma-Aldrich Chemie GmbH, Buchs, Switzerland respectively while $\text{K}_2[\text{PtCl}_4]$ was purchased from Alfa Aesar GmbH & Co KG, Karlsruhe, Germany. TiO_2 NPs (AEROXIDE TiO_2 P25) were purchased from Evonik Industries, Essen, Germany or Sigma-Aldrich Chemie GmbH, Buchs, Switzerland. Pristine ZrO_2 NPs (< 100 nm particle size) were purchased from Sigma-Aldrich Chemie GmbH, Buchs, Switzerland. For further characterization see ESI†. *cis*- $[\text{Ru}(\text{bpy})_2\text{Cl}_2]$ and anchoring ligand (**1**) were prepared according to the literature (see ESI† for synthetic details) [30–35]. Instrumentation details are given in the ESI†. Calculated major MALDI peaks given in the experimental sections were calculated using the most abundant isotopes (e.g., ^{102}Ru , ^{35}Cl).

2.2. Synthetic Procedures

2.2.1. TiO_2 NPs Functionalization

NP activation and functionalization with ligand (**1**) were carried out according to our previously published procedure [36,37]. The procedures were adjusted according to the molecular weight for anchoring ligand (**1**) (see following section).

2.2.2. Activation of Commercial P25 TiO_2 NPs

The commercially available NPs were activated as previously reported [36]. The procedure was scaled up as follows. Commercial P25 TiO_2 NPs (5.00 g) were dispersed by sonication for 15 min in dilute aqueous HNO_3 (70 mL, 3 M). The mixture was then stirred for 30 min. The suspension was centrifuged (10 min, 7000 rpm) and the NPs were washed once with milliQ water (70 mL). The NPs were added to milliQ water (50 mL) and dispersed by sonication for 10 min. The suspension was then stirred overnight. The suspension was centrifuged (10 min, 7000 rpm) and the NPs were washed with milliQ water (2×50 mL). The activated NPs (4.83 g) were stored in a sealed vial under N_2 after drying under high vacuum. TGA: weight loss/%, 1.8 (< 380 °C), 0.3 (380–900 °C). TGA-MS: amu, 18, 30 (< 380 °C), 18, 44 (380–900 °C). FTIR spectroscopy: 1607, 1582, 1427, and 1298 cm^{-1} . ICP-MS: No ruthenium or rhodium were detected in either the pristine or activated NPs.

2.2.3. Preparation of **1**@ TiO_2

The functionalization was performed as previously reported [36,37] with the procedure adjusted for the anchoring ligand 4,4'-bis(phosphonato)-2,2'-bipyridine as follows. (**1**) (25.0 mg, 0.079 mmol, 1 eq.) and milliQ water (18 mL) were added to a microwave vial and dispersed by sonication for 1 min. Activated TiO_2 NPs (727 mg, 33.9 TiO_2 eq.) were added. The suspension was dispersed by sonication for 10 min. The microwave vial was sealed, and the reaction mixture heated for 3 h at 130 °C in the microwave reactor. The suspension was centrifuged (20 min, 7000 rpm) after cooling to room temperature. The NPs were separated from the solvent. The white **1**@ TiO_2 NPs (742 mg) were stored in a sealed vial under N_2 after drying under high vacuum. For NMR spectroscopic measurements, **1**@ TiO_2 NPs (5–10 mg) were dispersed in 500 μL D_2O in an NMR tube. TGA: weight loss/%, 0.7 (< 380 °C), 2.9 (380–900 °C). TGA-MS: amu, 18 (< 380 °C), 18, 44 (380–900 °C). FTIR spectroscopy: 1630, 1590, 1540, 1500, 1480, 1430 and 1160 cm^{-1} . ICP-MS: No ruthenium or rhodium was detected. Solid-state absorption spectroscopy: 400–670 nm (weak). MALDI *m/z*: 317.1 [**1** + H]⁺ (calc. 317.0), 379.1 [**1** – H + TiO]⁺ (calc. 378.9), 445.0 [**1** + H + Ti_2O_2]⁺ (calc. 444.9) and 656.0 [**1**]₂ + H + Na]⁺ (calc. 656.0).

2.2.4. Ru@TiO₂

The metal complex was formed directly on the NP surface. Hence, **1**@TiO₂ (45.9 mg), RuCl₃·3H₂O (1.03 mg, 3.9 μmol), and 2,2'-bipyridine (1.56 mg, 10.0 μmol) were added to a vial. H₂O (5 mL) and EtOH (3 mL) were added, and the mixture was thoroughly dispersed using sonication and stirring. The suspension was transferred to an autoclave PTFE liner with additional EtOH (2 mL). The autoclave was sealed and then heated in an oven with 320 °C/h to 160 °C. The autoclave was left at 160 °C for 1 h. After cooling down the autoclave was opened and the suspension was centrifuged (20 min, 7000 rpm). The resulting NPs were washed with H₂O (3 × 10 mL) and EtOH (1 × 10 mL). Ru@TiO₂ was isolated as dark orange powder. ¹H-NMR spectroscopy, MALDI, TGA-MS, FTIR spectroscopy, ICP-MS, and solid absorption spectroscopy were performed on the NPs. TGA: weight loss/%, 1.5 (< 380 °C), 4.6 (380–900 °C). TGA-MS: amu, 18 (< 380 °C), 18, 44 (380–900 °C). FTIR spectroscopy: 1640, 1604, 1465, 1447, 1423, 1398, 1156, and 1049 cm⁻¹. ICP-MS: ruthenium present. Solid-state absorption spectroscopy: 400–490 nm, 490–700 nm (weak). MALDI *m/z*: 414.1 [Ru(bpy)₂]⁺ (calc. 414.0), 535.1 [Ru(**1**) + TiO₂ + K - 2 H]⁺ (calc. 534.8), 570.1 [Ru(**1**)(bpy) - 4 H]⁺ (calc. 569.9), 602.1 [Ru(bpy)₂ + CHCA - H]⁺ (calc. 602.1), 728.9 [Ru(**1**)(bpy)₂ - H]⁺ (calc. 729.0). (CHCA = α-cyano-4-hydroxycinnamic acid).

2.2.5. Ru@TiO₂ Using [Ru(bpy)₂Cl₂]

1@TiO₂ (45.9 mg) and [Ru(bpy)₂Cl₂] (3.05 mg, 5.0 μmol) were added to a vial. H₂O (5 mL) and EtOH (3 mL) were added, and the mixture was thoroughly dispersed using sonication and stirring. The suspension was transferred to an autoclave PTFE liner with additional EtOH (2 mL). The autoclave was sealed and then heated in an oven at a rate of 320 °C/h to 160 °C. The autoclave was left at 160 °C for 1 h. After cooling down, the autoclave was opened and the suspension was centrifuged (20 min, 7000 rpm). The resulting NPs were washed with H₂O (3 × 10 mL) and EtOH (1 × 10 mL). Ru@TiO₂ was isolated as an orange powder. ¹H-NMR spectroscopy, MALDI, TGA-MS, FTIR and solid absorption spectroscopy were performed on the NPs. TGA: weight loss/%, 0.6 (< 380 °C), 3.3 (380–900 °C). TGA-MS: amu, 18 (< 380 °C), 18, 44 (380–900 °C). FTIR spectroscopy: 1626, 1591, 1544, 1465, 1447, 1428, 1376 and 1155 cm⁻¹. Solid-state absorption spectroscopy: 400–490 nm, 490–700 nm (weak). MALDI *m/z*: 414.0 [Ru(bpy)₂]⁺ (calc. 414.0), 535.0 [Ru(**1**) + TiO₂ + K - 2 H]⁺ (calc. 534.8), 570.1 [Ru(**1**)(bpy) - 4 H]⁺ (calc. 569.9), 602.0 [Ru(bpy)₂ + CHCA - H]⁺ (calc. 602.1).

2.2.6. Rh@TiO₂

The metal complex was formed directly on the NP surface. **1**@TiO₂ (200 mg), RhCl₃·3H₂O (4.51 mg, 17.1 μmol) and 2,2'-bipyridine (6.81 mg, 4.36 μmol) were added to a vial. H₂O (5 mL) and EtOH (3 mL) were added, and the mixture was thoroughly dispersed using sonication and stirring. The suspension was transferred to an autoclave PTFE liner with additional EtOH (2 mL). The autoclave was sealed and then heated in an oven with 320 °C/h to 160 °C. The autoclave was left at 160 °C for 1 h. After cooling down the autoclave was opened and the suspension was centrifuged (20 min, 7000 rpm). The resulting NPs were washed with H₂O (3 × 10 mL) and EtOH (1 × 10 mL). Rh@TiO₂ was isolated as white powder. ¹H-NMR spectroscopy, MALDI, TGA-MS, FTIR spectroscopy, ICP-MS, and solid absorption spectroscopy were performed on the NPs. TGA: weight loss/%, 1.3 (< 380 °C), 3.8 (380–900 °C). TGA-MS: amu, 18 (< 380 °C), 18, 44 (380–900 °C). FTIR spectroscopy: 1633, 1607, 1544, 1500, 1470, 1453, 1401, 1378, and 1153 cm⁻¹. ICP-MS: rhodium present. Solid-state absorption spectroscopy: 400–440 nm, 440–700 nm (weak). MALDI *m/z*: 415.0 [Rh(bpy)₂]⁺ (calc. 415.0), 450.0 [Rh(bpy)₂ + Cl]⁺ (calc. 450.0), 603.1 [Rh(bpy)₂ + CHCA - H]⁺ (calc. 603.1) and 656.1 [(**1**)₂ + H + Na]⁺ (calc. 656.0).

2.2.7. rR-TiO₂

The metal complex was formed directly on the NP surface. Hence, **1**@TiO₂ (241 mg), RuCl₃·3H₂O (0.24 mg, 0.9 μmol), RhCl₃·3H₂O (5.16 mg, 19.6 μmol), and 2,2'-bipyridine (8.08 mg, 51.8 μmol) were added to a vial. H₂O (5 mL) and EtOH (3 mL) were added, and the mixture was thoroughly dispersed using sonication and stirring. The suspension was transferred to an autoclave PTFE liner with additional EtOH (2 mL). The autoclave was sealed and then heated in an oven at a rate of 320 °C/h to 160 °C. The autoclave was left at 160 °C for 1 h. After cooling down the autoclave was opened and the suspension was centrifuged (20 min, 7000 rpm). The resulting NPs were washed with H₂O (3 × 10 mL) and EtOH (1 × 10 mL). rR@TiO₂ was isolated as an orange powder. ¹H-NMR spectroscopy, MALDI, TGA-MS, FTIR spectroscopy, ICP-MS and solid absorption spectroscopy were performed on the NPs. TGA: weight loss/%, 1.1 (< 380 °C), 3.7 (380–900 °C). TGA-MS: amu, 18 (< 380 °C), 18, 44 (380–900 °C). FTIR spectroscopy: 1627, 1608, 1546, 1500, 1470, 1453, 1412, 1373 and 1149 cm⁻¹. ICP-MS: ruthenium and rhodium present. Solid-state absorption spectroscopy: 400–490 nm, 490–700 nm (weak). MALDI *m/z*: 415.0 [Rh(bpy)₂]⁺ (calc. 415.0), 450.0 [Rh(bpy)₂ + Cl]⁺ (calc. 450.0) and 603.1 [Rh(bpy)₂ + CHCA - H]⁺ (calc. 603.1).

2.2.8. RR-TiO₂

The metal complex was formed directly on the NP surface. **1**@TiO₂ (340 mg), RuCl₃·3H₂O (2.39 mg, 9.1 μmol), RhCl₃·3H₂O (5.16 mg, 19.6 μmol) and 2,2'-bipyridine (11.3 mg, 72.3 μmol) were added to a vial. H₂O (5 mL) and EtOH (3 mL) were added, and the mixture was thoroughly dispersed using sonication and stirring. The suspension was transferred to an autoclave PTFE liner with additional EtOH (2 mL). The autoclave was sealed and then heated in an oven with 320 °C/h to 160 °C. The autoclave was left at 160 °C for 1 h. After cooling down, the autoclave was opened and the suspension was centrifuged (20 min, 7000 rpm). The resulting NPs were washed with H₂O (3 × 10 mL) and EtOH (1 × 10 mL). RR-TiO₂ was isolated as a dark orange powder. ¹H-NMR spectroscopy, MALDI, TGA-MS, FTIR spectroscopy, ICP-MS and solid absorption spectroscopy were performed on the NPs. TGA: weight loss/%, 1.5 (< 380 °C), 3.5 (380–900 °C). TGA-MS: amu, 18 (< 380 °C), 18, 44 (380–900 °C). FTIR spectroscopy: 1643, 1542, 1498, 1472, 1447, 1423, 1398, 1375 and 1149 cm⁻¹. ICP-MS: ruthenium and rhodium present. Solid-state absorption spectroscopy: 400–490 nm, 490–700 nm (weak). MALDI *m/z*: 415.1 [Rh(bpy)₂]⁺ (calc. 415.0), 450.1 [Rh(bpy)₂ + Cl]⁺ (calc. 450.0), 603.1 [Rh(bpy)₂ + CHCA - H]⁺ (calc. 603.1) and 656.1 [(**1**)₂ + H + Na]⁺ (calc. 656.0), 729.1 [Ru(**1**)(bpy)₂ - H]⁺ (calc. 729.0).

2.2.9. Preparation of **1**@ZrO₂

The functionalization was performed as previously reported [36,37] without the acid treatment activation step. The procedure was further adjusted for the anchoring ligand 4,4'-bis(phosphonato)-2,2'-bipyridine and a different NP surface as follows. (**1**) (20.0 mg, 0.063 mmol, 1 eq.) and milliQ water (18 mL) were added to a microwave vial and dispersed by sonication for 1 min. ZrO₂ NPs (897 mg, 6.9 ZrO₂ eq.) were added. The suspension was dispersed by sonication for 10 min. The microwave vial was sealed, and the reaction mixture heated for 3 h at 130 °C in the microwave reactor. The suspension was centrifuged (20 min, 7000 rpm) after cooling to room temperature. The NPs were separated from the solvent and washed with H₂O (3 × 10 mL) and EtOH (1 × 10 mL). The white **1**@ZrO₂ NPs (856 mg) were stored in a sealed vial under N₂ after drying under high vacuum. For NMR spectroscopic measurements, **1**@ZrO₂ NPs (5–10 mg) were dispersed in 500 μL D₂O in an NMR tube. TGA: weight loss/%, 0.6 (< 380 °C), 1.7 (380–900 °C). TGA-MS: amu, 18 (< 380 °C), 18, 44 (380–900 °C). FTIR spectroscopy: 1625, 1590, 1542, 1496, 1473, 1432, 1376, 1223, 1152, 1038, 1000, 840, 744, 658, 562 and 480 cm⁻¹.

2.2.10. Ru@ZrO₂

The metal complex was formed directly on the NP surface. Hence, **1**@ZrO₂ (142 mg), RuCl₃·3H₂O (2.07 mg, 7.9 μmol), and 2,2'-bipyridine (2.50 mg, 16.0 μmol) were added to a vial. H₂O (5 mL) and EtOH (3 mL) were added, and the mixture was thoroughly dispersed using sonication and stirring. The suspension was transferred to an autoclave PTFE liner with additional EtOH (2 mL). The autoclave was sealed and then heated in an oven with 320 °C/h to 160 °C. The autoclave was left at 160 °C for 1 h. After cooling down the autoclave was opened and the suspension was centrifuged (20 min, 7000 rpm). The resulting NPs were washed with H₂O (3 × 10 mL) and EtOH (1 × 10 mL). Ru@ZrO₂ was isolated as an ochre powder. ¹H-NMR spectroscopy, MALDI, TGA-MS and FTIR spectroscopy were performed on the NPs. TGA: weight loss/%, 0.6 (< 380 °C), 2.1 (380–900 °C). TGA-MS: amu, 18 (< 380 °C), 18, 44 (380–900 °C). FTIR spectroscopy: 1644, 1604, 1544, 1465, 1447, 1422, 1398, 1223, 1160, 1122, 1057, 913, 744, 658, 562, and 480 cm⁻¹.

2.2.11. rR-ZrO₂

The metal complex was formed directly on the NP surface. Hence, **1**@ZrO₂ (366 mg), RuCl₃·3H₂O (0.24 mg, 0.9 μmol), RhCl₃·3H₂O (5.16 mg, 19.6 μmol) and 2,2'-bipyridine (6.45 mg, 41.3 μmol) were added to a vial. H₂O (5 mL) and EtOH (3 mL) were added, and the mixture was thoroughly dispersed using sonication and stirring. The suspension was transferred to an autoclave PTFE liner with additional EtOH (2 mL). The autoclave was sealed and then heated in an oven with 320 °C/h to 160 °C. The autoclave was left at 160 °C for 1 h. After cooling down the autoclave was opened and the suspension was centrifuged (20 min, 7000 rpm). The resulting NPs were washed with H₂O (3 × 10 mL) and EtOH (1 × 10 mL). rR@ZrO₂ was isolated as light orange powder. ¹H-NMR spectroscopy, MALDI, TGA-MS and FTIR spectroscopy were performed on the NPs. TGA: weight loss/%, 0.4 (< 380 °C), 2.1 (380–900 °C). TGA-MS: amu, 18 (< 380 °C), 18, 44 (380–900 °C). FTIR spectroscopy: 1633, 1606, 1589, 1541, 1498, 1468, 1452, 1429, 1398, 1375, 1215, 1156, 1042, 1000, 910, 839, 744, 658, 562, and 480 cm⁻¹.

2.3. Dihydrogen Generation

2.3.1. General Procedure

The system for dihydrogen generation used metal complex functionalized NPs [38] as photo- and electrocatalysts, triethanolamine as a sacrificial electron donor, K₂[PtCl₄] as catalyst to facilitate dihydrogen formation (possibly by Pt NP formation), bpy as additive, aqueous H₂SO₄ for pH adjustment, and milliQ water as solvent. As [Ru(bpy)₃]²⁺ and [Rh(bpy)₃]³⁺ are somewhat photolabile under the operating conditions, the additional bpy was added to regenerate ruthenium and rhodium surface-bound complexes.

In a 5 mL microwave vial TEOA (2.52 mmol, 376 mg), K₂[PtCl₄] (1.7 μmol, 0.70 mg) and 2,2'-bipyridine (18.6 μmol, 2.91 mg) were added together with milliQ water and aqueous H₂SO₄ (1M) to modify the pH. Experiments performed at pH 10 used no aqueous H₂SO₄ (1M) and 6 mL milliQ water while experiments performed at pH 7.5 used 1 mL aqueous H₂SO₄ (1M) and 5 mL milliQ water. Metal complex-functionalized NPs were added (114.1 mg). The vial was flushed with nitrogen and then sealed. The suspension was sonicated (10 min) and thoroughly shaken. Nitrogen was bubbled through the suspension for 10 min. The vial was irradiated for 4–8 h at a slight angle (5°) with a sun simulator generating 1200 W m⁻². The suspension was shaken hourly. Headspace samples for gas chromatography were collected using a syringe and transferred to a 10 mL GC vial for analysis. The measured GC integral was converted to mL of H₂ with a calibration made by injecting several known volumes of dihydrogen.

2.3.2. Kinetic Measurements

Using the general procedure, a kinetic run was performed at pH 7.5 using rR@TiO₂ as photocatalyst. Two vials were prepared and the H₂ evolution was measured hourly by collecting the headspace by syringe and transferring it to a 10 mL GC vial for GC analysis. After each collection, the suspension was bubbled with N₂ for 5 min and then irradiation was continued. The vials were irradiated in total for 8 h and 9 h respectively.

2.3.3. Recycle Measurements

Using the general procedure, a recycling experiment was performed preparing two vials at pH 7.5 using rR@TiO₂ as photocatalyst with 4 h irradiation for each cycle. H₂ evolution was recorded after each cycle by collecting the headspace by syringe and transferring it to a 10 mL GC vial for GC analysis. After each collection, the suspension was centrifuged, the supernatant was removed, the NPs were washed with water (4 × 10 mL). Subsequently, the NPs were dried under high vacuum. Following the general procedure, the recycled NPs were used instead for the next cycle.

3. Results and Discussion

3.1. Ligand Functionalization, Surface Complexation and Material Characterisation

3.1.1. Anchoring Ligand Functionalization

We commenced by establishing a reliable method for the preparation of 1@TiO₂ and its subsequent metallation. Anchoring ligand **1** was prepared according to the literature [31–35] with the phosphonic acid being chosen for stable binding to TiO₂ surfaces in neutral, slightly basic and slightly acidic conditions [36,37]. The bpy metal-binding domain in **1** is commensurate with the assembly of surface-bound $\{M(\text{bpy})_3\}^{n+}$ (M = Ru, $n = 2$; M = Rh, $n = 3$) motifs. The previously developed method [36,37] for NP anchor functionalization with tpy metal-binding domains was adapted for anchoring ligand **1**. In this case, 32.2 eq. of activated NPs [38,39] were dispersed with anchoring ligand **1** in water and heated to 130 °C for 3 h in a microwave reactor (see Experimental section for full details).

The purchased ZrO₂ NPs were functionalized using similar techniques but without prior activation. The ZrO₂ NPs had a diameter of 100 nm changing the surface area to volume ratio significantly (from 28% to 6%). The functionalization method was optimized using our previously established formula [38] to give an adjusted ratio of 6.9 ZrO₂ eq. to 1 eq. anchoring ligand. The resulting NPs were carefully washed to avoid non-bound free ligand.

3.1.2. Ligand Functionalized NP Characterisation Methods

The 1@TiO₂ NPs were analysed using TGA-MS (see Figure S1) and showed a small weight loss (< 1%) in two steps (< 120 °C, < 380 °C) attributed to the loss of physisorbed and chemisorbed water. This was further seen in the coupled MS, which showed peaks with m/z of 17 and 18 for HO and H₂O respectively. A further weight loss of 2.9% over the range of 380–900 °C was measured and attributed to the decomposition of the anchoring ligand on the surface. The MS in this range showed the decomposition product of the ligand to be CO₂. In contrast, activated NPs (see Figure S2) showed almost no weight loss over the range of 380–900 °C. To verify that the organic weight loss within the 380–900 °C range was not caused by non-covalently bound free ligand, the ¹H NMR spectrum of 1@TiO₂ was measured in D₂O (see Figure S3) and showed no significant amounts of free ligand in solution (ligand bound to the NPs is not observed) [36]. Further characterisation with FTIR spectroscopy (see Figure S4) and solid-state absorption spectroscopy (see Figure S5) revealed peaks at 1630, 1590, 1540, 1500, 1480, 1430, and 1160 cm⁻¹ and 400–670 nm respectively which are not observed for pristine activated NPs. The additional peaks found for 1@TiO₂ in FTIR spectroscopy did match to the pristine anchoring ligand. MALDI mass spectrometry showed peaks arising from species consistent with surface binding of the phosphonate ligand (See Figures S6–S8).

$1@ZrO_2$ was characterized similarly to $1@TiO_2$: TGA-MS, 1H NMR spectroscopy, and FTIR spectroscopy (see Figures S9–S12) were measured. $1@ZrO_2$ showed a weight loss of 1.7% over the range of 380–900 °C, which was attributed to the decomposition of the anchoring ligand on the surface. The MS in this range showed the decomposition product of the ligand to be CO_2 . The commercial NPs did not show any weight loss other than H_2O . 1H NMR spectroscopy in D_2O was used to verify absence of non-covalently bound free ligand and no significant amounts of free ligand in solution were observed. FTIR spectroscopy showed several weak additional peaks compared to the commercial NPs within the 1600 and 800 cm^{-1} region (see ESI† Figure S12) originating from the anchoring ligand.

3.1.3. Nanoparticle Surface Complexation

Metal complexes were assembled directly on the NP surface using methods derived from literature procedures for heteroleptic ruthenium(II) complexes, replacing free ligand by $1@TiO_2$ (Table 2) [35]. Orange $Ru@TiO_2$ was isolated from the reaction of $1@TiO_2$ NPs [38], $RuCl_3 \cdot 3H_2O$, and bpy in 1:1 water-ethanol in an autoclave at 160 °C for 1 h (see Experimental section for full details). $Ru@TiO_2$ can also be formed by replacing $RuCl_3 \cdot 3H_2O$ and bpy with $[Ru(bpy)_2Cl_2]$, giving a similar product (TGA-MS, 1H NMR spectroscopy, FTIR and solid-state absorption spectroscopies, MALDI mass spectrometry see Figures S13–S27) differing only slightly in colour and small weight loss differences during the TGA measurement. All subsequent metal complex-functionalized NPs (Table 2) were prepared in the autoclave with $H_2O/EtOH$ as solvent using the one-pot ($MCl_3 + bpy$) procedure described in the experimental. The abbreviation $rR@TiO_2$ describes metal complex functionalized NPs with a small amount of ruthenium vs. rhodium (1:20) on the surface, while for $RR@TiO_2$ ruthenium and rhodium surface concentrations are comparatively similar (1:2). The first letter in rR and RR always refers to ruthenium and the second to rhodium.

Table 2. Different metal complex functionalized nanoparticles.

Entry	$1@TiO_2$ ^a	$RuCl_3$	$RhCl_3$	bpy
$Ru@TiO_2$	1.0 eq.	0.79 eq.	0	2.0 eq.
$Rh@TiO_2$	1.0 eq.	0	0.79 eq.	2.0 eq.
$rR@TiO_2$	1.0 eq.	0.04 eq.	0.76 eq.	2.0 eq.
$RR@TiO_2$	1.0 eq.	0.25 eq.	0.54 eq.	2.0 eq.

^a $1@TiO_2$ equivalents represent estimated amount of **1** on the NP surface.

The metal complexes $Ru@ZrO_2$ and $rR@ZrO_2$ were prepared using $1@ZrO_2$ as starting material and followed the procedure described above with TiO_2 .

3.1.4. Complex Functionalized Characterisation Methods

All metal complex-functionalized NPs species were characterized using the same methods as $1@TiO_2$. For both $Ru@TiO_2$ and $Rh@TiO_2$, TGA-MS (Figures S13 and S28) confirmed a higher weight loss (380–900 °C) than $1@TiO_2$. 1H NMR spectroscopy (Figures S15 and S29) showed that no labile species were adsorbed on the NPs. In contrast to $1@TiO_2$, FTIR spectroscopy (Figures S16 and S30) showed absorptions between 1650 and 1590 cm^{-1} in addition to 1540, 1470, 1450, 1400, and 1150 cm^{-1} originating from the organic ligands. Solid-state absorption spectroscopy showed broad and weak absorptions between 400 and 670 nm. Additionally $Rh@TiO_2$ showed a more pronounced absorption band at 420 nm (Figure S31), whilst any surface bound ruthenium complex gave dominant absorptions between 410 and 490 nm (Figure S17). The MALDI mass spectrum of $Rh@TiO_2$ (see Figures S32–S35) showed masses with the correct isotope pattern at m/z : 415.0 $[Rh(bpy)_2]^+$ (calc. 415.0), 450.0 $[Rh(bpy)_2 + Cl]^+$ (calc. 450.0), 603.1 $[Rh(bpy)_2 + CHCA - H]^+$ (calc. 603.1) and 656.1 $[(1)_2 + H + Na]^+$ (calc. 656.0), while that of $Ru@TiO_2$ (Figures S18–S27) showed masses with the correct isotope patterns at m/z : 414.1 $[Ru(bpy)_2]^+$ (calc. 414.0), 535.1 $[Ru(1)$

+ TiO₂ + K - 2 H]⁺ (calc. 534.8), 570.1 [Ru(1)(bpy) - 4 H]⁺ (calc. 569.9), 602.1 [Ru(bpy)₂ + CHCA - H]⁺ (calc. 602.1), 728.9 [Ru(1)(bpy)₂ - H]⁺ (calc. 729.0). For NPs containing both ruthenium and rhodium, the observed isotope distribution in the MALDI mass spectrum confirmed that the rhodium complex was dominant (Figures S36–S44). For full characterisation details, see Section 2 or ESI† Figures S36–S49.

Emission spectra of the metal complex functionalized NPs dispersed in water were recorded (Figure 1). The suspension was excited at 450 nm. Ru@TiO₂ showed a broad emission at 634 nm while RR@TiO₂ showed a broad emission at 630 nm. Both Rh@TiO₂ and rR@TiO₂ were non-emissive.

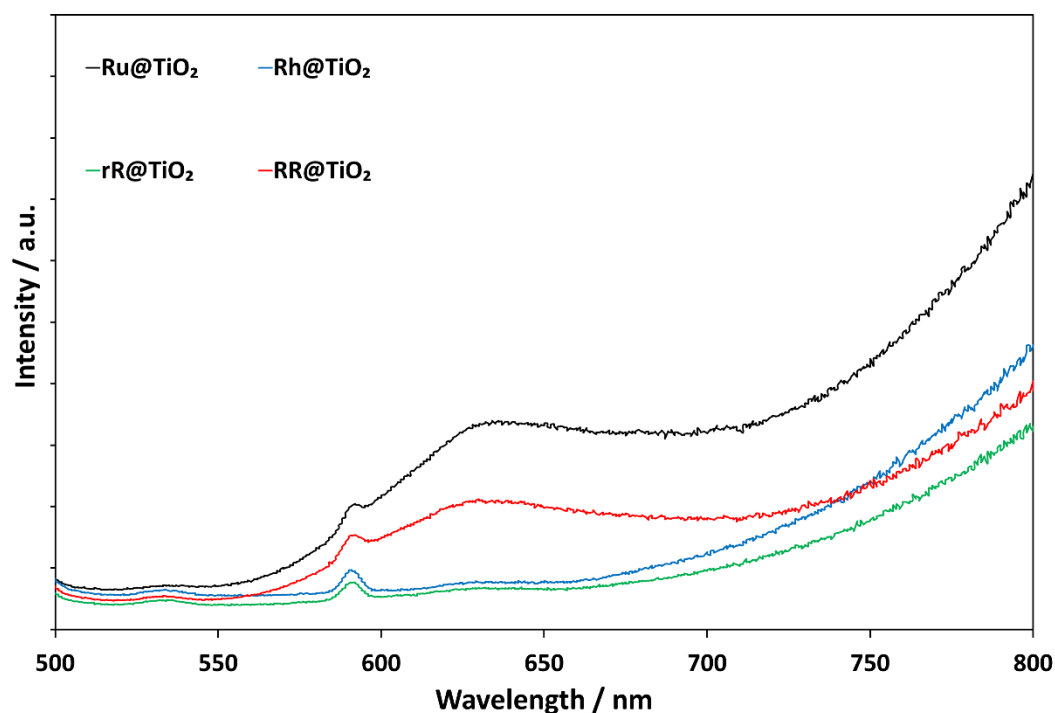


Figure 1. Emission spectra of complex-functionalized NPs after excitation at 450 nm. Excitation slit width 3 nm, emission slit width 10 nm.

The NPs were further investigated using ICP-MS (see Table 3). Ruthenium or rhodium functionalized NPs showed their respective elements. It was not possible to perform an exact surface concentration measurement of the elements with ICP-MS as even concentrated nitric acid did not remove all of the surface-bound species from the NP.

Table 3. ICP-MS concentration and standard deviation of functionalized TiO₂ NPs.

Sample	⁴⁷ Ti Conc. µg/L	⁴⁷ Ti Conc. RSD ^a	¹⁰¹ Ru Conc. µg/L	¹⁰¹ Ru Conc. RSD ^a	¹⁰³ Rh Conc. µg/L	¹⁰³ Rh Conc. RSD ^a	⁸⁹ Y (ISTD) Conc. µg/L	⁸⁹ Y (ISTD) Conc. RSD ^a
c-NPs	16,756.5	6.1	0.1	17.7	0.1	5.5	145,600.3	4.0
a-NPs	21,460.7	5.6	0.3	127.0	0.3	106.3	150,634.5	4.6
1@TiO ₂	20,492.8	4.7	0.1	12.8	0.1	2.9	146,834.6	5.6
Ru@TiO ₂	21,142.6	21.0	232.7	2.4	0.1	4.0	141,660.1	5.1
Rh@TiO ₂	21,879.5	5.7	0.2	9.6	117.7	3.6	148,959.7	5.3
rR@TiO ₂	20,350.4	2.6	22.2	3.1	89.6	2.5	142,814.2	5.4
RR@TiO ₂	18,659.6	5.9	62.0	4.2	53.5	2.9	146,352.9	5.9
rR@TiO ₂ ^b	13,466.9	2.9	3.5	3.2	3.1	4.5	142,412.9	6.5

^a Relative standard deviation in percentage, triplicate measurements, ⁸⁹Y used as internal standard to account for matrix effects, ^b rR@TiO₂ after 10 dihydrogen catalytic cycles were measured.

For Ru@ZrO₂ and rR@ZrO₂, characterization was performed using TGA-MS, ¹H NMR spectroscopy, and FTIR spectroscopy (see Figures S12 and S50–S52). TGA-MS of Ru@ZrO₂ and rR@ZrO₂ revealed a smaller weight loss of 2.1% (380–900 °C) compared to the TiO₂ equivalents Ru@TiO₂ (4.6%) and rR@TiO₂ (3.7%). This was within expectations considering the weight loss seen for 1@ZrO₂. Importantly, an increase from 1@ZrO₂ to Ru@ZrO₂ or rR@ZrO₂ was still observed. ¹H NMR spectroscopy was used to verify the absence of non-bound anchoring ligand while the FTIR spectra showed only minor differences to 1@ZrO₂ within 1600–800 cm⁻¹.

3.2. Dihydrogen Generation

3.2.1. Performance and Influence of Individual Components during Dihydrogen Generation

Experimental details are given in Section 2.3.1. The study revealed that 1@TiO₂, Ru@TiO₂, and Rh@TiO₂ all produce H₂ under irradiation (Table 4) but the gas generation is significantly higher when both ruthenium and rhodium are present on the surface. It is especially interesting that when a single batch of NPs was functionalized with both metal complexes (rR@TiO₂ or RR@TiO₂), the H₂ production was more than double compared to that using an equivalent mixture of Ru@TiO₂ and Rh@TiO₂. We propose that the additional efficiency for rR@TiO₂ and RR@TiO₂ can be explained by an energy transfer from Ru to Rh which promotes the dihydrogen generation [27,40]. The recorded emission spectra of each species support this proposal as rR@TiO₂ is not emissive. It has to be noted that the energy transfer must be relatively inefficient since with higher ruthenium concentrations on the surface (RR@TiO₂ vs. rR@TiO₂) the metal complex functionalized NPs are emissive again.

Table 4. Performed dihydrogen generating experiments; see Table 2 for NP abbreviations.

Entry No.	NPs / μmol	Byp / μmol	pH	Time /h	GCI ^a /a. u.	H ₂ /mL (mL h ⁻¹)
1	Ru@TiO ₂ /1.5	18.6	10	8	152,250	3.14 (0.39)
2	Rh@TiO ₂ /9.3	18.6	10	8	199,140	4.11 (0.51)
3 ^b	Ru@TiO ₂ + Rh@TiO ₂ /9.7	18.6	10	8	255,530	5.27 (0.66)
4	rR@TiO ₂ /9.7	18.6	10	8	451,170	9.30 (1.16)
5	rR@TiO ₂ /9.7	18.6	7.5	4	455,940	9.40 (2.34)
6	rR@TiO ₂ /9.7	0	7.5	4	332,280	6.85 (1.71)
7 ^c	rR@TiO ₂ /9.7	18.6	7.5	4	34,720	0.50 (0.13)
8	RR@TiO ₂ /9.7	18.6	7.5	4	384,200	7.92 (1.98)
9 ^d	RR@TiO ₂ /13.0	18.6	7.5	4	398,860	8.23 (2.06)
10 ^d	RR@TiO ₂ /13.0	210	7.5	4	397,710	8.20 (2.05)
11 ^e	a-NP	18.6	7.5	4	138,600	2.86 (0.71)
12	1@TiO ₂ /12.2	18.6	7.5	4	134,050	2.76 (0.69)
13	0	18.6	7.5	4	0	0.00 (0.00)
14 ^f	rR@TiO ₂ /9.7	18.6	7.5	4	533,930	11.0 (2.75)
15 ^g	rR@TiO ₂ /9.7	18.6	7.5	4	318,210	6.5 (1.64)
16 ^f	rR@ZrO ₂ /9.7	18.6	7.5	4	29,720	0.6 (0.15)
17 ^h	rR@TiO ₂ /9.7	0	7.5	4	88,360	1.82 (0.46)

^a GC integral (GCI) was adjusted for pre-existing nitrogen headspace in the reaction vial and partial sampling during the GC measurement, ^b using Ru@TiO₂ (5.1 mg) and Rh@TiO₂ (109 mg), ^c no K₂[PtCl₄] used, ^d vial headspace was measured after 2h and 4h irradiation, generated H₂ was added together, ^e 114.1 mg a-NP were used, ^f vial was stirred instead of shaken hourly, ^g vial was irradiated using normal sunlight instead, ^h using 18.6 mmol phen as additive.

Further experiments were performed to test the influence of each component in the system. In the absence of K₂[PtCl₄], there was a strong decrease in efficiency while

$K_2[PtCl_4]$ on its own gave no H_2 generation. Removing bpy had a less significant influence on the H_2 generation but slightly lowered the efficiency. In contrast, increasing the bpy concentration had no effect on the efficiency. TEOA was essential for dihydrogen formation. Another important parameter was the pH; at pH 10 the system generated dihydrogen at half the rate observed at pH 7.5. A pH dependence is expected as the formal driving force of the reaction (ΔG) will depend upon pH according to the Nernst equation ($\Delta G = -nFE$) since the key step in the formation of H_2 involves a proton. A significant improvement in H_2 formation (17%, $TOF_{Rh} = 3.4 \times 10^{-3} s^{-1}$, $TOF_{Ru} = 7.4 \times 10^{-2} s^{-1}$) could be observed by simple stirring of the suspension instead of periodic shaking. This shows when the metal complex functionalized NPs settle and block the light, they partially hinder a successful water reduction on covered NPs. For this observation to be possible, a successful surface functionalization must have happened. A further experiment was performed by using normal sunlight, resulting in respectable dihydrogen generation (see Table 4, Entry 15 [§]), especially since the weather conditions were not bright sunlight.

The dihydrogen generation experiment was expanded using ZrO_2 NPs as the metal complex carrier material. Since ZrO_2 is an insulator, the change from TiO_2 (band gap = 3.2 eV) [28] to ZrO_2 (band gap = 5.1 eV) [29] was expected to hinder the H_2 generation during the experiment if the metal complex is surface-bound and interacting electronically with the NP. Hence, the experiment (see Table 4, Entry 16 [§]) yielding almost no H_2 generation during the irradiation was interesting and strongly implies mediation by the semiconducting TiO_2 nanoparticles.

3.2.2. Kinetics of $rR@TiO_2$ during Light Irradiation

The kinetics of the H_2 formation when using $rR@TiO_2$ in the general setup was investigated and the experimental results are plotted in Figure 2a) and shown in Table 5. Experimental details are given in Section 2.3.2. Analysis of the data in Figure 2 when TEOA was considered as a reactant (see Figure 2b) indicated first order kinetics ($R_2 = 0.986$) or second order kinetics ($R_2 = 0.995$). This observation is consistent with the mechanism proposed by Kirch et al. [27]. Using these data, a minimal TON of 86 ($TOF = 2.7 \times 10^{-3} s^{-1}$) and TON 1844 ($TOF = 5.7 \times 10^{-2} s^{-1}$) can be calculated for the rhodium and ruthenium surface-bound complexes respectively. Furthermore, the amount of H_2 produced after 9 h irradiation corresponds to a depletion of 32% of TEOA.

Table 5. Performed hourly kinetic dihydrogen generating experiment of two sample vials.

Runtime/h	GC Integral ^a S1	H ₂ Generated S1	GC Integral ^a S2	H ₂ Generated S2
	/a. u.	/mL	/a. u.	/mL
1	146,050	3.04	171,190	3.57
2	154,530	3.22	172,650	3.60
3	143,060	2.92	136,850	2.85
4	112,380	2.34	95,670	1.99
5	90,960	1.89	83,770	1.75
6	82,450	1.72	81,480	1.70
7	61,900	1.29	80,410	1.67
8	69,260	1.44	62,050	1.29
9	52,740	1.33	-	-

^a GC integrals were adjusted for pre-existing nitrogen headspace in the reaction vial and partial sampling during the GC measurement.

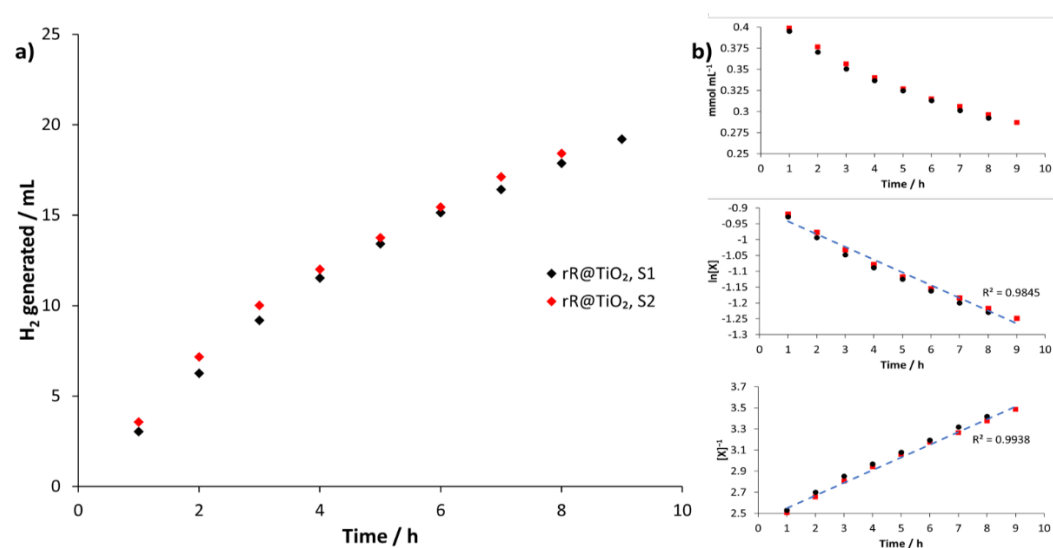


Figure 2. (a) Graphical representation of H₂ generated using rR@TiO₂ in mL during light irradiation experiments versus time for two samples. (b) Zeroth order reaction graph (**top**), concentration (mmol per mL) starting material during kinetic irradiation measurements of two samples (red and black) against time (hours); 1st order reaction graph (**middle**), natural logarithm of starting material concentration [X] during kinetic irradiation measurements of two samples (red and black) against time (hours), linear trendline through datapoints (blue); 2nd order reaction graph (**bottom**), One over concentration [X] of starting material during kinetic irradiation measurements of two samples (red and black) against time (hours), linear trendline through data points (blue).

3.2.3. Recyclability of rR@TiO₂

Our motivation was to develop a system that could be recycled multiple times and still generate dihydrogen upon irradiation (see Video 1 in the ESI† for visual representation). After an initial run, the NPs were separated from the solution and washed several times with water to ensure the complete removal of the solution components. The NPs were then dried under high vacuum and redispersed in milliQ water at pH 7.5 with fresh TEOA, bpy and K₂[PtCl₄]. After each run, the headspace was collected and measured using GC analysis (see Table 6). Overall, rR@TiO₂ NPs were most suitable for multiple cycles with only a slight decline in efficiency (see Figure 3). We believe that the decline in efficiency is due to the loss of NPs in the recycling processing (10 wt.% after 8 cycles) and defunctionalization of the NP surface. Using the data, a minimal TON of 300 (TOF = $1.9 \times 10^{-3} \text{ s}^{-1}$) and TON 6424 (TOF = $4.1 \times 10^{-2} \text{ s}^{-1}$) can be calculated for the rhodium(III) and ruthenium(II) surface bound complexes, respectively.

Table 6. Performed recycle dihydrogen generating experiments of two sample vials.

Cycle/N	GC Integral ^a /a. u.	NPs Runtime/h	H ₂ /mL (mL h ⁻¹)
0	455,940	4	9.40 (2.35)
1	463,320	8	9.55 (2.38)
2	372,850	12	7.68 (1.92)
3	344,720	16	7.10 (1.77)
4	277,740	20	5.73 (1.43)
5	258,630	24	5.33 (1.33)
6	257,160	28	5.30 (1.33)
7	228,530	32	4.71 (1.18)
8	209,710	36	4.32 (1.08)
9	191,940	40	3.96 (0.99)
10	181,590	44	4.75 (0.94)

^a GC integrals were adjusted for pre-existing nitrogen headspace in the reaction vial and partial sampling during the GC measurement.

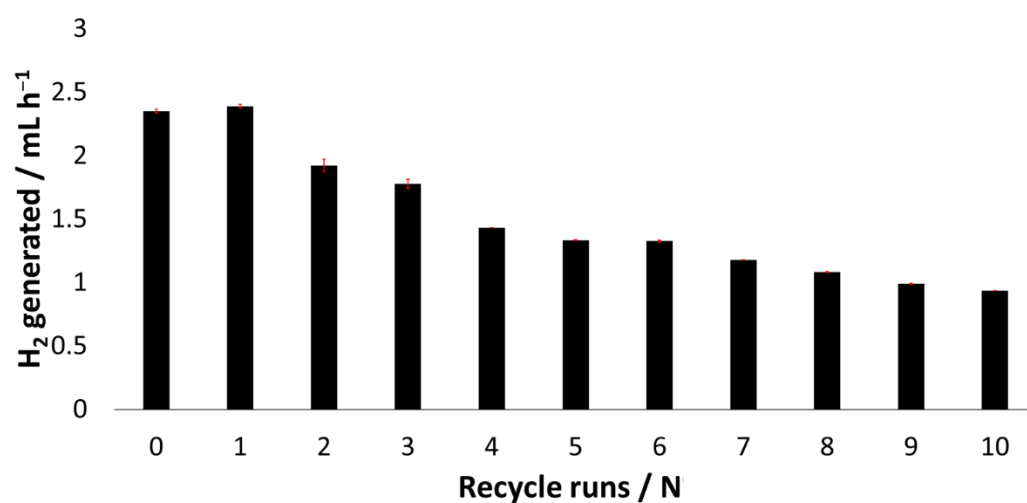


Figure 3. Graphical representation of dihydrogen generated measured through GC analysis after each cycle using rR@TiO₂ as photocatalyst, standard deviation indicated with red error bars.

4. Conclusions

We have demonstrated the immobilization of an established photochemical system for the solar generation of dihydrogen using sunlight by binding photo- and redox-active Rh and Ru complexes to TiO₂ NP surfaces. We further show that binding both metal complexes to the same NP improves the photocatalytic efficiency. The kinetic rate order and recyclability were determined. The NPs could be recycled multiple times and retain dihydrogen generation capacity. TON and TOF of the system were determined and exceeded the previous reported similar homogenous system. The dihydrogen generation was monitored using GC while the NPs were characterized using various methods, including MALDI, FTIR spectroscopy, TGA-MS, solid-absorption spectroscopy, fluorescence emission spectroscopy, and ICP-MS.

Supplementary Materials: The following supporting information can be downloaded at: www.mdpi.com/article/10.3390/nano12050789/s1. Details of instrumentation and procedure, experimental to anchoring synthesis. Video S1: Visible H₂ formation during irradiation. Scheme S1: Anchoring Ligand Synthesis route. Figures S1–S8: TGA-MS (activated NPs, 1@TiO₂), ¹H NMR spectroscopy (1@TiO₂), solid state IR spectra (activated NPs, 1@TiO₂, 1), solid state absorption spectra (1@TiO₂) and MALDI mass spectra (1@TiO₂). Figures S9–S12: TGA-MS (pristine ZrO₂, 1@ZrO₂), ¹H NMR spectroscopy (1@ZrO₂), solid state IR spectra (pristine ZrO₂, 1@ZrO₂, Ru@ZrO₂ and rR@ZrO₂). Figures S13–S27: TGA-MS, ¹H NMR spectroscopy, solid state IR spectra, solid state absorption spectra and MALDI mass spectra for Ru@TiO₂ made with RuCl₃·3 H₂O and *cis*-[Ru(bpy)₂Cl₂]. Figures S28–S35: TGA-MS, ¹H NMR spectroscopy, solid state IR spectra, solid state absorption spectra and MALDI mass spectra for Rh@TiO₂. Figures S36–S49: MALDI mass spectra (rR@TiO₂, RR@TiO₂) TGA-MS (rR@TiO₂, RR@TiO₂), ¹H NMR spectroscopy (rR@TiO₂, RR@TiO₂), solid state IR spectra (activated NPs, 1@TiO₂, rR@TiO₂, RR@TiO₂) and solid state absorption spectra (1@TiO₂, Ru@TiO₂, Rh@TiO₂, rR@TiO₂, RR@TiO₂). Figures S50–S52: TGA-MS (Ru@ZrO₂ and rR@ZrO₂) and ¹H NMR spectroscopy (Ru@ZrO₂ and rR@ZrO₂).

Author Contributions: Methodology, investigation, formal analysis, writing—original draft, S.A.F.; writing review and editing, C.E.H. and E.C.C.; supervision, project management, funding acquisition, C.E.H. and E.C.C. All authors have read and agreed to the published version of the manuscript.

Funding: This research was funded by Swiss National Science Foundation, grant number 200020_182000.

Data Availability Statement: Data are available from the authors on request.

Acknowledgments: We acknowledge support from the University of Basel. We would like to thank Markus Lenz (FHNW, Muttensz, Basel) for carrying out the ICP-MS measurements.

Conflicts of Interest: The authors declare no conflict of interest.

References

1. Omer, A.M. Energy, environment and sustainable development. *Renew. Sustain. Energy Rev.* **2008**, *12*, 2265–2300. <https://doi.org/10.1016/j.rser.2007.05.001>.
2. Bölük, G.; Mert, M. Fossil & renewable energy consumption, GHGs (greenhouse gases) and economic growth: Evidence from a panel of EU (European Union) countries. *Energy* **2014**, *74*, 439–446. <https://doi.org/10.1016/j.energy.2014.07.008>.
3. Letcher, T.M. 1—Introduction With a Focus on Atmospheric Carbon Dioxide and Climate Change. In *Future Energy: Improved, Sustainable and Clean Options for Our Planet*, 3rd ed.; Letcher, T.M., Ed.; Elsevier: Amsterdam, The Netherlands, 2020; pp. 3–17.
4. Metzger, J.O.; Hüttermann, A. Sustainable global energy supply based on lignocellulosic biomass from afforestation of degraded areas. *Sci. Nat.* **2009**, *96*, 279–288. <https://doi.org/10.1007/s00114-008-0479-4>.
5. Kang, J.-N.; Wei, Y.-M.; Liu, L.-C.; Han, R.; Yu, B.-Y.; Wang, J.-W. Energy systems for climate change mitigation: A systematic review. *Appl. Energy* **2020**, *263*, 114602. <https://doi.org/10.1016/j.apenergy.2020.114602>.
6. Rivard, E.; Trudeau, M.; Zaghbi, K. Hydrogen Storage for Mobility: A Review. *Materials* **2019**, *12*, 1973. <https://doi.org/10.3390/ma12121973>.
7. Available online: <https://www.rsc.org/periodic-table/element/1/hydrogen> (accessed on 14 June 2021).
8. Timmerberg, S.; Kaltschmitt, M.; Finkbeiner, M. *Hydrogen and Hydrogen-Derived Fuels through Methane Decomposition of Natural Gas—GHG Emissions and Costs*; Elsevier: Amsterdam, The Netherlands, 2020; Volume 7, p. 100043.
9. Wang, S.; Lu, A.; Zhong, C.-J. Hydrogen production from water electrolysis: Role of catalysts. *Nano Converg.* **2021**, *8*, 4. <https://doi.org/10.1186/s40580-021-00254-x>.
10. Chen, L.; Qi, Z.; Zhang, S.; Su, J.; Somorjai, G.A. Catalytic Hydrogen Production from Methane: A Review on Recent Progress and Prospect. *Catalysts* **2020**, *10*, 858. <https://doi.org/10.3390/catal10080858>.
11. Dovì, V.G.; Friedler, F.; Huisingh, D.; Klemesš, J.J. Cleaner energy for sustainable future. *J. Clean. Prod.* **2009**, *17*, 889–895. <https://doi.org/10.1016/j.jclepro.2009.02.001>.
12. Johnson, T.C.; Morris, D.J.; Wills, M. Hydrogen generation from formic acid and alcohols using homogeneous catalysts. *Chem. Soc. Rev.* **2010**, *39*, 81–88. <https://doi.org/10.1039/B904495G>.
13. Sajjadi, S.; Khataee, A.; Darvishi Cheshmeh Soltani, R.; Hasanzadeh, A. N, S co-doped graphene quantum dot-decorated Fe₃O₄ nanostructures: Preparation, characterization and catalytic activity. *J. Phys. Chem.* **2019**, *127*, 140–150. <https://doi.org/10.1016/j.jpccs.2018.12.014>.
14. Hassan, A.F.; Elhadidy, H. Effect of Zr⁴⁺ doping on characteristics and sonocatalytic activity of TiO₂/carbon nanotubes composite catalyst for degradation of chlorpyrifos. *J. Phys. Chem.* **2019**, *129*, 180–187. <https://doi.org/10.1016/j.jpccs.2019.01.018>.
15. Maleki, A.; Taheri-Ledari, R.; Ghalavand, R.; Firouzi-Haji, R. Palladium-decorated o-phenylenediamine-functionalized Fe₃O₄/SiO₂ magnetic nanoparticles: A promising solid-state catalytic system used for Suzuki–Miyaura coupling reactions. *J. Phys. Chem.* **2020**, *136*, 109200. <https://doi.org/10.1016/j.jpccs.2019.109200>.
16. Stevens, P.D.; Fan, J.; Gardimalla, H.M.R.; Yen, M.; Gao, Y. Superparamagnetic Nanoparticle-Supported Catalysis of Suzuki Cross-Coupling Reactions. *Org. Lett.* **2005**, *7*, 2085–2088. <https://doi.org/10.1021/ol050218w>.
17. Zecchina, A.; Bordiga, S.; Groppo, E. *Selective Nanocatalysts and Nanoscience: Concepts for Heterogeneous and Homogeneous Catalysis*; Wiley-VHC: Weinheim, Germany, 2011.
18. Samira Bagheri, N.M.J. *Nanocatalysts in Environmental Applications*; Springer: Cham, Switzerland, 2018.
19. Albonetti, S.; Mazzoni, R.; Cavani, F. CHAPTER 1 Homogeneous, Heterogeneous and Nanocatalysis. In *Transition Metal Catalysis in Aerobic Alcohol Oxidation*; Green Chemistry Series; Cardona, F., Parmeggiani, C., Eds.; RSC: London, UK, 2015; pp. 1–39.
20. Kumaravel, V.; Imam, M.D.; Badreldin, A.; Chava, R.K.; Do, J.Y.; Kang, M.; Abdel-Wahab, A. Photocatalytic Hydrogen Production: Role of Sacrificial Reagents on the Activity of Oxide, Carbon, and Sulfide Catalysts. *Catalysts* **2019**, *9*, 276. <https://doi.org/10.3390/catal9030276>.
21. Yoong, L.S.; Chong, F.K.; Dutta, B.K. Development of copper-doped TiO₂ photocatalyst for hydrogen production under visible light. *Energy* **2009**, *34*, 1652–1661. <https://doi.org/10.1016/j.energy.2009.07.024>.
22. Kanade, K.G.; Kale, B.B.; Baeg, J.-O.; Lee, S.M.; Lee, C.W.; Moon, S.-J.; Chang, H. Self-assembled aligned Cu doped ZnO nanoparticles for photocatalytic hydrogen production under visible light irradiation. *Mater. Chem. Phys.* **2007**, *102*, 98–104. <https://doi.org/10.1016/j.matchemphys.2006.11.012>.
23. Chowdhury, P.; Gomaa, H.; Ray, A.K. Sacrificial hydrogen generation from aqueous triethanolamine with Eosin Y-sensitized Pt/TiO₂ photocatalyst in UV, visible and solar light irradiation. *Chemosphere* **2015**, *121*, 54–61. <https://doi.org/10.1016/j.chemosphere.2014.10.076>.
24. Popugaeva, D.; Tian, T.; Ray, A.K. Hydrogen production from aqueous triethanolamine solution using Eosin Y-sensitized ZnO photocatalyst doped with platinum. *Int. J. Hydrog. Energy* **2020**, *45*, 11097–11107. <https://doi.org/10.1016/j.ijhydene.2020.02.055>.
25. Zuo, F.; Wang, L.; Wu, T.; Zhang, Z.; Borchardt, D.; Feng, P. Self-Doped Ti³⁺ Enhanced Photocatalyst for Hydrogen Production under Visible Light. *J. Am. Chem. Soc.* **2010**, *132*, 11856–11857. <https://doi.org/10.1021/ja103843d>.
26. Romero, N.; Guerra, R.B.; Gil, L.; Drouet, S.; Salmeron-Sánchez, I.; Illa, O.; Philippot, K.; Natali, M.; García-Antón, J.; Sala, X. TiO₂-mediated visible-light-driven hydrogen evolution by ligand-capped Ru nanoparticles. *Sustain. Energy Fuels* **2020**, *4*, 4170–4178. <https://doi.org/10.1039/D0SE00446D>.

27. Kirch, M.; Lehn, J.-M.; Sauvage, J.-P. Hydrogen Generation by Visible Light Irradiation of Aqueous Solutions of Metal Complexes. An approach to the photochemical conversion and storage of solar energy. *Helv. Chim. Acta* **1979**, *62*, 1345–1384. <https://doi.org/10.1002/hlca.19790620449>.
28. Ansari, S.A.; Cho, M.H. Highly Visible Light Responsive, Narrow Band gap TiO₂ Nanoparticles Modified by Elemental Red Phosphorus for Photocatalysis and Photoelectrochemical Applications. *Sci. Rep.* **2016**, *6*, 25405. <https://doi.org/10.1038/srep25405>.
29. Singh, H.; Sunaina; Yadav, K.K.; Bajpai, V.K.; Jha, M. Tuning the bandgap of m-ZrO₂ by incorporation of copper nanoparticles into visible region for the treatment of organic pollutants. *Mater. Res. Bull.* **2020**, *123*, 110698. <https://doi.org/10.1016/j.materresbull.2019.110698>.
30. Lenis-Rojas, O.A.; Fernandes, A.R.; Roma-Rodrigues, C.; Baptista, P.V.; Marques, F.; Pérez-Fernández, D.; Guerra-Varela, J.; Sánchez, L.; Vázquez-García, D.; Torres, M.L.; et al. Heteroleptic mononuclear compounds of ruthenium(II): Synthesis, structural analyses, in vitro antitumor activity and in vivo toxicity on zebrafish embryos. *Dalton Trans.* **2016**, *45*, 19127–19140. <https://doi.org/10.1039/C6DT03591D>.
31. Zhang, D.; Telo, J.P.; Liao, C.; Hightower, S.E.; Clennan, E.L. Experimental and Computational Studies of Nuclear Substituted 1,1'-Dimethyl-2,2'-Bipyridinium Tetrafluoroborates. *J. Phys. Chem. A* **2007**, *111*, 13567–13574. <https://doi.org/10.1021/jp074323u>.
32. Maerker, G.; Case, F.H. The Synthesis of Some 4,4'-Disubstituted 2,2'-Bipyridines. *J. Am. Chem. Soc.* **1958**, *80*, 2745–2748. <https://doi.org/10.1021/ja01544a042>.
33. Han, W.-S.; Han, J.-K.; Kim, H.-Y.; Choi, M.J.; Kang, Y.-S.; Pac, C.; Kang, S.O. Electronic Optimization of Heteroleptic Ru(II) Bipyridine Complexes by Remote Substituents: Synthesis, Characterization, and Application to Dye-Sensitized Solar Cells. *Inorg. Chem.* **2011**, *50*, 3271–3280. <https://doi.org/10.1021/ic101909e>.
34. Montalti, M.; Wadhwa, S.; Kim, W.Y.; Kipp, R.A.; Schmehl, R.H. Luminescent Ruthenium(II) Bipyridyl-Phosphonic Acid Complexes: pH Dependent Photophysical Behavior and Quenching with Divalent Metal Ions. *Inorg. Chem.* **2000**, *39*, 76–84. <https://doi.org/10.1021/ic991143t>.
35. Norris, M.R.; Concepcion, J.J.; Glasson, C.R.K.; Fang, Z.; Lapidés, A.M.; Ashford, D.L.; Templeton, J.L.; Meyer, T.J. Synthesis of Phosphonic Acid Derivatized Bipyridine Ligands and Their Ruthenium Complexes. *Inorg. Chem.* **2013**, *52*, 12492–12501. <https://doi.org/10.1021/ic4014976>.
36. Freimann, S.A.; Zare, D.; Housecroft, C.E.; Constable, E.C. The SALSAC approach: Comparing the reactivity of solvent-dispersed nanoparticles with nanoparticulate surfaces. *Nanoscale Adv.* **2020**, *2*, 679–690. <https://doi.org/10.1039/C9NA00488B>.
37. Freimann, S.A.; Prescimone, A.; Housecroft, C.E.; Constable, E.C. Turning over on sticky balls: Preparation and catalytic studies of surface-functionalized TiO₂ nanoparticles. *RSC Adv.* **2021**, *11*, 5537–5547. <https://doi.org/10.1039/D0RA09319J>.
38. The surface area-to-volume ratio of NPs with an average radius of 10.5 nm is 28%. Surface concentrations were calculated as 0.28 times the number of TiO₂ formula equivalents. When describing experiments using functionalized NPs, the number of equivalents or moles refer to the estimated amount of anchoring ligand or complex bound to the surface using the above formula.
39. Available online: <https://www.aerosil.com/sites/lists/RE/DocumentsSI/TI-1243-Titanium-Dioxide-as-Photocatalyst-EN.pdf>. (accessed on 5 April 2020).
40. Cooke, M.W.; Santoni, M.-P.; Loiseau, F.; Hasenknopf, B.; Hanan, G.S. Energy transfer in rhodium–ruthenium dimer-of-dimer assemblies. *Inorg. Chim. Acta* **2017**, *454*, 208–215. <https://doi.org/10.1016/j.ica.2016.05.034>.